Comparing *E* field changes aloft to lightning mapping data

Richard G. Sonnenfeld,[1] John Battles,[1,2] Gaopeng Lu,[1] and William P. Winn[1]

Received 28 February 2006; revised 14 June 2006; accepted 31 July 2006; published XX Month 2006.

[1] A newly developed balloon-borne instrument contains electric and magnetic sensors for determining how lightning alters electric field vectors relative to a coordinate system fixed with the Earth. By combining results from this instrument with results from the compact Lightning Mapping Array (LMA) at Langmuir Laboratory in central New Mexico and the National Lightning Detection Network (NLDN), charge transported to ground by several strokes in a cloud-to-ground (CG) lightning flash can be quantified. As the flash progresses, the locations of the charge centers drained by successive strokes are seen to move further from the ground-strike point. Using this new instrument and two different models to map LMA source points onto charge centers, the charge transported in an intracloud (IC) flash is also estimated. Details of the instrument design and data analysis are also presented.

Citation: Sonnenfeld, R. G., J. Battles, G. Lu, and W. P. Winn (2006), Comparing *E* field changes aloft to lightning mapping data, *J. Geophys. Res.*, *111*, XXXXXX, doi:10.1029/2006JD007242.

1. Introduction

[2] In the past decade, arrays of radio receivers for reconstructing the time evolution and locations of lightning channels have become more widely available, and thus it is now possible to observe lightning propagation inside thunderclouds where we cannot see it with optical instruments. One important instrument of this type is called the lightning mapping array (LMA) [*Rison et al.*, 1999; *Krehbiel et al.*, 2000]. While the view of lightning presented by the LMA and similar instruments is illuminating, it does not tell us specifically about the main effect of lightning, which is to move electrical charge from place to place by providing conducting paths in air for electrical currents.

[3] In this paper we introduce a balloon-borne instrument (called Esonde) to detect the rapid variations of the electric field vector resulting from lightning flashes. The electric field sensors, or electrodes, are four metal patches on the outside of the cylindrical housing of the instrument (Figure 1). The metal patches are electrically insulated from the housing, but they are connected with wires to amplifiers and data storage media inside the cylinder. The electric field strength at the surface of each sensor induces an electrical charge on each sensor. The locations of the sensors are chosen so that the relative amounts of induced charge are different for electric vectors in different directions. The induced electric charges can be used to find the variation of the electric vector in a reference frame relative to the instrument. The variation of the electric vector relative to Earth can be determined from magnetic sensors in the instrument for finding the orientation of the instrument. With simultaneous information about the location of lightning channels as mapped by the LMA, it is possible to deduce some aspects of the movement of electrical charge.

[4] Each of the four electrodes and associated circuits constitutes a type of instrument variously called an "electric-field-change meter" or a "slow antenna," and thus the whole instrument can be described as an array of four slow antennas. The word "slow" describes the ability of an amplifier attached to a sensor to respond to low frequencies; in our instrument, the gain of the amplifiers declines below about 1 Hz.

[5] *Thomson et al.* [1988a, 1988b] describe an instrument functionally similar to ours to study charge carried by lightning channels near the ground. Their electrode patches reside on the surface of a metallic sphere instead of a cylinder. More recently, *Beasley et al.* [2000] incorporated a single slow antenna into a balloon-borne instrument designed to measure X rays from lightning. Only distant lightning was present during the flight, according to K. Eack (private communication, Dec. 2005).

[6] Arrays of widely separated slow antennas at the surface of the Earth have been used to study how lightning moves electrical charge. In the late 1970s eight slow antennas were used in New Mexico and Florida to find both the amounts and locations of electrical charges lowered to ground [*Krehbiel et al.*, 1979; *Uman et al.*, 1978]. For charge moved from one place to another inside a cloud, at least seven slow antennas were required. Now, when locations of lightning channels are determined by a lightning mapping array, it is possible to quantify the movement of charge with fewer instruments. Here we explore what is possible with a single balloon-borne instrument for finding the directions and magnitudes of electric vectors.

[1] Department of Physics and Langmuir Laboratory, New Mexico Institute of Mining and Technology, Socorro, New Mexico, USA.

[2] Now at Space Instrumentation and Systems Engineering, Los Alamos National Laboratory, Los Alamos, New Mexico, USA.

0148-0227/06/2006JD007242$09.00

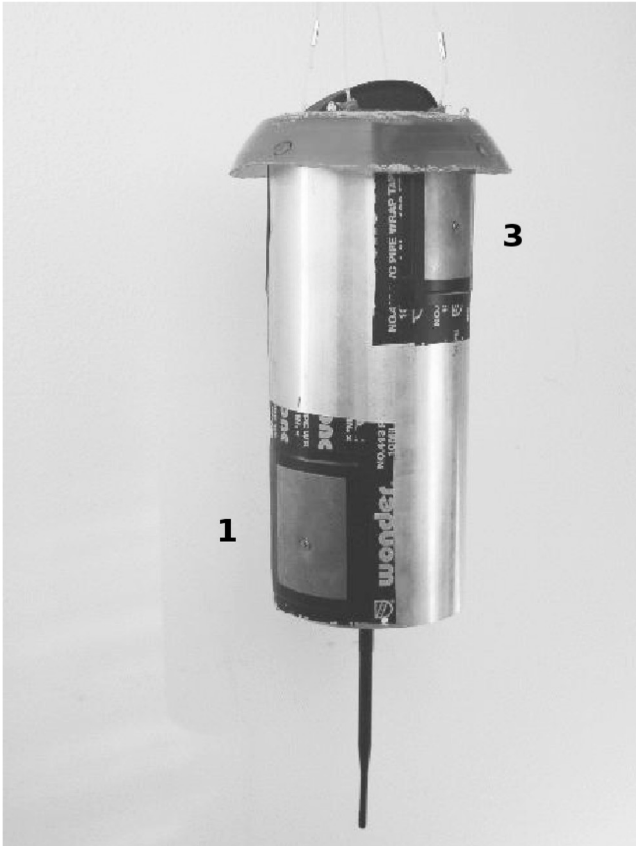

Figure 1. In this Esonde photo, the charge sense plate identified as **3** is at top right, while plate **1** is at bottom left. Pipe wrap tape isolates the plates from the cylinder. A single screw in the middle of each plate attaches it electrically to its amplifier. The GPS is a black bulge on top, and the dipole telemetry antenna protrudes beneath the main cylinder.

[7] The balloon-borne instrument in combination with a lightning mapping array and the National Lightning Detection Network (a facility operated by Vaisala Corporation), can be used to continue past work to quantify the total amounts of charge relocated by lightning. More significantly, it can also be used to study the distribution of charge along a single branch of a lightning channel when lightning passes near the balloon. Examples of both uses are presented below after a more complete description of the instrument.

2. Instrument Design

2.1. Mechanical Overview

[8] Figure 1 provides an external view of the Esonde. The body of the instrument is a 370-mm high cylinder of 75-mm radius covered with 0.5-mm thick 6061-T6 sheet aluminum. The four electrodes, made of 0.3-mm-thick brass sheet, are rectangles 112 mm tall by 90 mm wide. The electrodes are arranged in two pairs. The upper pair is aligned with the Esonde's y axis, and the lower pair with the x axis. Each electrode subtends an angle of roughly 70 °. The electrode centers are separated by 230 mm along the long axis (z axis) of the Esonde. The electrodes are insulated from the cylinder with 0.010-inch-thick pipe-wrap tape. A single screw captures each electrode and binds it to a nylon support attached to a brass nut. This nut is permanently wired to the charge amplifier input for each electrode. The instrument shell (the main cylinder) provides the common reference for the analog signals.

[9] The flight-ready package has a mass of 2.7 kg. Each circuit board within is mounted to an aluminum disk. The aluminum disks are stacked with spacers between on four steel support rods. While the 18-8 steel alloy used in the support rods is weakly ferromagnetic, it has been found experimentally that it is not sufficiently magnetic to interfere with B field measurements.

2.2. Electronic Subsystems

[10] The computer is a Prometheus PR-Z32-EAZ-ST from Diamond Systems Corporation. It combines a full personal computer with an analog-to-digital (A/D) converter on a single 10 cm × 10 cm circuit board in a PC-104 configuration. In operation, it consumes less than 5 W. The sigma-delta A/D converter yields 16-bit resolution at 100 kHz total sample rate. A 16:1 analog multiplexer ahead of the A/D converter receives analog signals from the electric, magnetic, and other sensors. Eight of the channels are sampled 10,000 times a second (f_S = 10000, ΔT_S = 100 μs), while the other eight channels are sampled roughly three times in a minute to log slowly changing data such as temperature and battery voltages.

[11] The multiplexed approach is less expensive and lighter weight than a dedicated A/D converter per data channel, but requires that all analog sensors have sufficiently low output impedance to fully charge the A/D converter within the sample window. Otherwise, data on a given channel may be contaminated by residual voltage from the channel just scanned by the multiplexer. A multiplexed A/D converter also leads to interchannel time skew. More will be said about skew later.

[12] The three-axis flux-gate magnetometer is Model 113 made by Applied Physics Systems. It has a sensitivity of 4 V/gauss, operates on ±5 V, and has a frequency response up to 400 Hz. It consumes only 150 mW in operation. Table 1 shows averages of 10 min of B field measurements while the Esonde is flying in a storm near Langmuir Lab. Table 1 also shows results from a detailed model of the Earth's B field, the International Geomagnetic Reference Field. (Results of this model for any location on Earth may be obtained from the British Geological Survey

Table 1. Comparing Measured to Modeled B Field[a]

Magnetic Field at Latitude 33.97°, Longitude −107.18°, Altitude 3250 m	Model IGRF	Measured
Total field B	0.498 gauss	0.493 ± .01
Vertical field B_z	0.437 gauss	0.437 ± .01
Transverse field B_T	0.239 gauss	0.227 ± .01
Inclination θ_I	−61.26°	−62.5° ± 1.0
Declination ϕ_D	10.05°	not measured

[a]Measured inclination (θ_B) is defined in equation (12). The model used is the 10th version of the International Geomagnetic Reference Field (IGRF). The modeled results correspond to the values predicted at the latitude, longitude and altitude of Langmuir Lab during August of 2004.

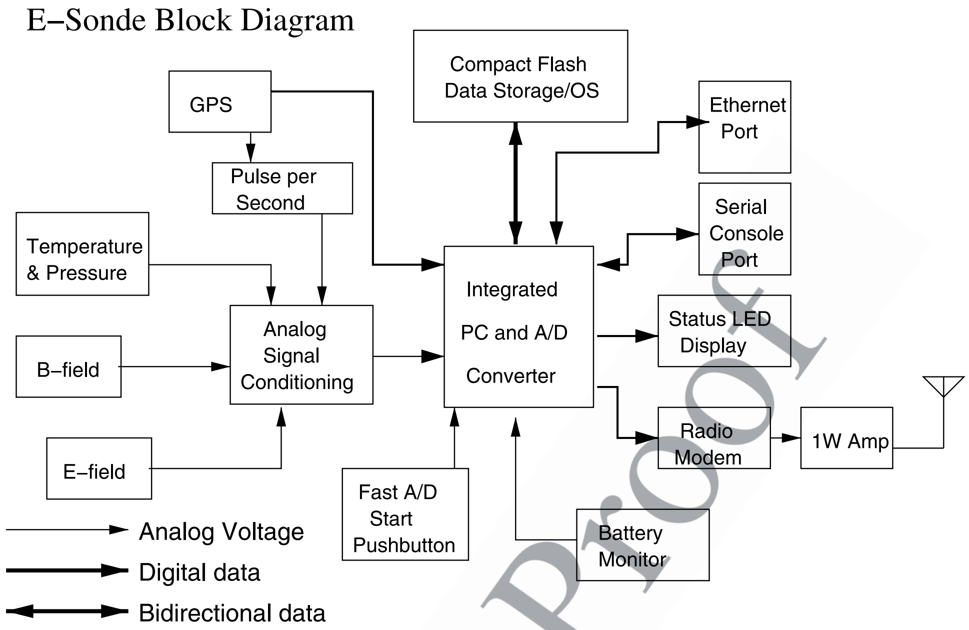

Figure 2. The Esonde is built around a small but complete personal computer on the same board as a 16-channel multiplexed analog-to-digital converter. This block diagram shows that all analog signals are integrated at a signal-conditioning board and fed via ribbon cable to the A/D converter. The compact flash unit contains the data acquisition program and space for the acquired data. Software selects a subset of science data for telemetry. Ethernet and serial ports allow logging into the package up until a minute before launch. The primary lithium cells give a run time of 7 hours. Battery and voltage regulator subsystems are not shown.

at http://www.geomag.bgs.ac.uk/gifs/igrf_form.shtml.) The Esonde's measurements are in good agreement with the model, providing some confidence in the use of magnetic sensor data in the calculation of Esonde orientation.

[13] The Global Positioning System (GPS) receiver is a Garmin GPS-35LVS low-voltage unit with integrated antenna designed for marine applications. It streams data out a serial port and has a separate output with one pulse per second, which, for precise timing, is digitized by the A/D converter on the Prometheus board along with other analog signals.

[14] Telemetry is simplified with the use of a MaxStream X09-019WNI spread-spectrum transmitter operating around 900 MHz and capable of transmitting 19.2 kbaud serial data to a companion unit on the ground. We increased the usable range of the telemetry by using a Yagi receiving antenna. The transmitting antenna on the balloon-borne instrument is a 1/2-wavelength whip antenna, which is visible in Figure 1.

[15] The charge amplifier circuit has an LT-1058ISW operational amplifier manufactured by Linear Technology, Inc., which was chosen because it has a fast slew rate. With the feedback capacitor and resistors used in the circuit, a step increase in charge on the associated electrode produces a step in the output voltage that decays away with a characteristic time of 1 s. The decay can be removed in the data analysis over the time interval of a lightning flash, but an unknown constant remains. This means that changes in induced charge can be measured, but the constant induced charge caused by relatively constant cloud background E fields remains unknown.

2.3. Instrument Integration

[16] The data rate of the telemetry transmitter, 19.2 kbaud, is not sufficient to handle the fast data rate required for studying lightning. Thus data are stored in flash memory in the balloon-borne instrument while the telemetry transmits GPS coordinates so the instrument can be recovered. The telemetry also transmits electric field components at a reduced data rate and other information about the health of the instrument.

[17] The computer uses the Linux operating system, which resides in less than 100 MBytes of a 1-GByte compact-flash (CF) card. The remainder of the memory is available for data. At 160 kBytes/s, the instrument records data throughout the flight in cycles lasting roughly 3 s. During the first 2.0 s of the cycle, data are acquired by the computer, and then during the last 1.0 s, data are not acquired while the computer writes to the compact flash memory card, and sometimes transmits results. The software can be rewritten to save only the data from lightning flashes, thereby avoiding the 1.0 s dead time and allowing a greater sampling frequency, but our initial effort is to evaluate the noise level throughout the flight and to learn how to detect automatically the presence of lightning.

[18] Figure 2 is a block diagram of the electronic components. The serial ports on the Prometheus computer (labeled "Integrated PC and A/D Converter" in Figure 2) are used to communicate with the GPS receiver and the telemetry system. All analog signals come together at a signal conditioning board ahead of the A/D converter. Power is provided by 20 AA primary lithium cells. The networking capability of the computer facilitates prelaunch checkout,

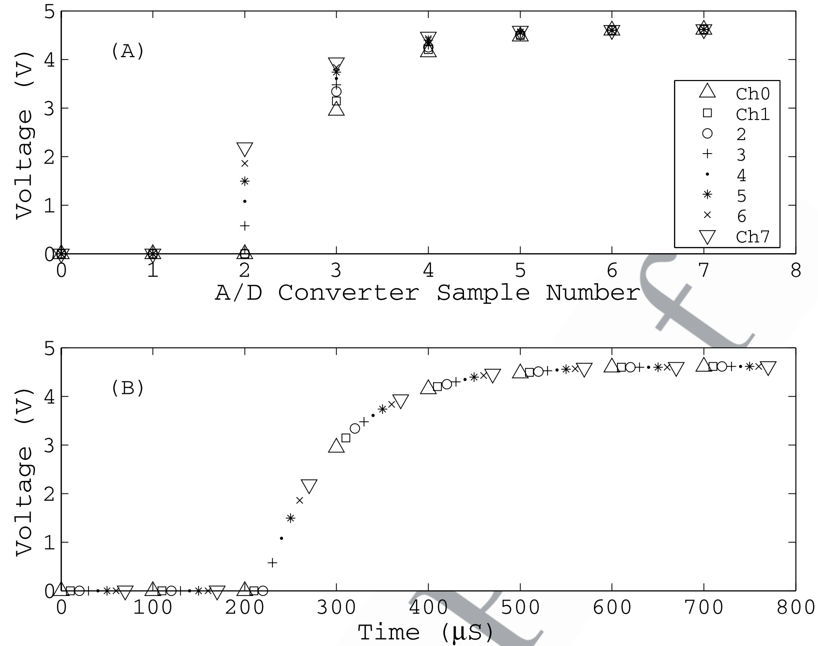

Figure 3. The eight fast A/D channels on the Prometheus are temporarily hooked together to illustrate the method for subsample time resolution. (a) The voltage versus sample number is shown. For a given sample number, channel 0 is sampled first, followed by channels 1–7. The PPS signal is broadened by an RC filter with a time constant of 75 μs. (b) The same voltages, represented by the same symbols, are assigned proper times, on the basis of the known A/D interchannel skew. Channel 0 is assumed to occur on a multiple of 100 μs. Subsequent samples are each separated by 10 μs from their predecessor. After all channels 0–7 have been sampled, there is a 30 μs reset time, then the sampling begins again with channel 0. Since we know the sampling pattern of the A/D converter and the shape of the rising PPS pulse, the start time of the PPS pulse can be calculated more accurately than the 100 μs intersample time.

customization of the data acquisition routines and instrument calibration.

2.4. Timing

[19] Comparing the electric field vectors obtained by the Esonde with lightning locations from the Lightning Mapping Array (LMA) requires coordinated timing. As both LMA and Esonde use GPS-based timing, it is useful to define Err_t^{LMA} and Err_t^{ES} to represent the error of LMA and Esonde times from GPS-based universal time. According to *Thomas et al.* [2004], $Err_t^{LMA} \ll 1\ \mu\ s$. The sampling frequency f_S of the Esonde is f_S = 10 kSamples/s, and the intrasample time $\Delta T_S = 1/f_S = 100\ \mu$s. To make best use of the data at this frequency, it is necessary for the Esonde time error (Err_t^{ES}) to be comparable to ΔT_S. There is nothing that can be done with the current hardware to reduce ΔT_S. However, since errors in experimental data from multiple sources sum in quadrature to produce errors larger than each individual error, there is some small further benefit if $Err_t^{ES} \ll \Delta T_S$. The following discussion details how this is accomplished.

[20] We verified in the lab that the GPS-35LVS used in our instrument is accurate to $Err_{PPS}^{GPS} < 1\ \mu$s at the pulse-per-second (PPS) output. The GPS also outputs text characters with the current time via a serial port. The timing uncertainty for this serial character output is $Err_{serial}^{GPS} \simeq 0.1$ s. The serial character output is less accurate than the PPS output because the GPS puts out only $\simeq$500 characters/s.

[21] The Prometheus computer on the Esonde inherits the Network Time Protocol (NTP) from the Linux operating system. Ordinarily, computers on the ground use NTP by communicating with remote NTP computer servers that are connected to GPS receivers or other time standards. The Prometheus computer, during a balloon flight, cannot be connected to the internet, but it can nonetheless run NTP disciplined by the timing emitted from the serial port of the GPS receiver on the Esonde. The more accurate PPS output from the GPS was not used to discipline NTP, as it does not specify which second is the present one; it only specifies when the present second begins. Tests confirmed that NTP disciplined by the GPS serial output kept the computer clock accurate to within 0.1 s.

[22] While 0.1 s accuracy of time-stamping would allow one to identify the same flash with both Esonde and LMA, it is not precise enough to compare the details of the flash as seen by the two instruments. So, first, each data packet is stamped with the character time-string generated by the NTP-disciplined computer clock. This assures the data packet is identified with the proper second. Second, to more precisely locate the beginning of that second, the computer is programmed to digitize the pulse-per-second output from the GPS receiver along with the analog data. Though the intrinsic pulse rise time is of order 1 μs, benefit is gained by broadening the pulse with a simple RC filter with time constant τ = 75 μs. Figure 3 provides additional detail on how the PPS is used to accurately time stamp all data.

Table 2. Definition of Variables Used in Discussion of How to Calculate Earth-Referenced E Field Components From Measurements the Instrument Makes

Variable Name	Description
V_0, V_1, V_2, V_3	voltages from charge amplifiers
E_{Sx}, E_{Sy}, E_{Sz}	E field components in Esonde frame
E_x, E_y, E_z	E field components in Earth frame (the $+E_x$ direction is east, $+E_y$ direction is North, $+E_z$ is up)
B_{Sx}, B_{Sy}, B_{Sz}	Earth B field components in Esonde frame
B	magnitude of Earth's B field
ϕ_B	counterclockwise angle from electrode 0 to magnetic north
ϕ_T	counterclockwise angle from electrode 0 to true north
ϕ	counterclockwise angle from due east to vector **E**
θ_B	measured inclination (Esonde frame)
θ_I	inclination angle (Earth frame)
ϕ_D	declination angle (Earth frame)

[23] Our computer digitizes eight fast analog channels: one for PPS, three for magnetic field components, and four for the electric field sensing electrodes. The data of Figure 3 were obtained by connecting all eight fast analog-to-digital converter inputs (A/D channels 0–7) to the RC-filtered pulse-per-second line. Figure 3a shows the voltage on the filtered PPS line at the beginning of the second when the line goes high. All eight channels read zero at sample 0 and sample 1 of Figure 3a, but at sample 2 the PPS pulse begins and increasing channel numbers read increasing voltages. If the Prometheus used eight independent A/D channels, the voltages on each of the channels would be identical. The increasing readings shown in Figure 3a are the effect of a single A/D being multiplexed at a frequency $f_M \simeq 10 f_S$. There is a time skew of roughly $1/f_M$ = 10 μs between channels. Figure 3b makes more sense of the Figure 3a data by explicitly including this time skew into the time axis of the plot. One clearly sees the total sample time for all 8 fast-data channels is T_S = 100 μs; which is composed of seven 10-μs intervals followed by a 30-μs hardware reset time. Further, inspection of Figure 3a should convince one that there will always be at least one point (e.g., sample number 2) for which the filtered PPS edge will have a magnitude between 20% and 80% of this maximum. Knowing this maximum value, the very simple shape of the RC rise curve, and the magnitude at sample 2, we predict the time at which the pulse began to rise from zero (e.g., 220 μs in Figure 3b). The Esonde data timestamps are created in postprocessing using these predicted pulse times. The four channels that are combined to produce electric field data occur $\simeq$10 μs apart as shown. The time stamp used corresponds to the time at which channel 1 is digitized. There is a further (verified) assumption that the sample time ΔT_S is constant to at least one part in 10^5 for periods of a second. The result is that Esonde data time stamps are correct to an accuracy of $Err_t^{ES} \simeq \Delta T_S/5$ = 20 μs. If the GPS-PPS output had not been filtered, one would know only that it had changed from low to high sometime between samples. This would mean $Err_t^{ES} \simeq \Delta T_S/2$. By filtering the PPS output, and knowing its pulse shape, the algorithm described produces a more accurate time stamp.

[24] In summary, the 1 pulse-per-second output from the GPS receiver precisely marks the beginning of each second, while the NTP slaved to the same receiver gives a character string which uniquely identifies the second just passed in Universal Time (UT). Filtering, then fitting, the GPS PPS allows Esonde and LMA data to be compared to an accuracy $Err_t^{ES} < T_S$.

2.5. Instrument Calibration

[25] As there will be much discussion from here on of electric field components as seen in different reference frames it is important to distinguish E_{Sx}, the x component of **E** in the Esonde reference frame, from E_x, the x component of **E** in the reference frame of the Earth. Refer to Table 2 for complete definitions of variables used in this section.

[26] The instrument is a segment of a cylinder with four sensing electrodes, two of which are visible in Figure 1. We define the z axis to be upward along the axis of symmetry of the cylinder. The x axis is perpendicular to the axis of symmetry in the direction from the center of electrode **1** to the center of electrode **0**, the lower pair of electrodes. The y axis is perpendicular to both the z and x axes and points in the direction from electrode **3** to electrode **2**, the upper pair of electrodes. The xyz axes form a right-handed coordinate system.

[27] Calibration to find the E_{Sx} and E_{Sy} components of the electric vector can be worked out from electrostatic theory using the approximation that the ends of the cylinder are far from the electrodes [*Pugh and Pugh*, 1970]. In this approximation, the charge density around the circumference of the cylinder arising from the E_{Sx} component, for example, is

$$\sigma_x = 2\epsilon_0 E_{Sx} \cos\alpha \ , \tag{1}$$

where $\epsilon_0 = 8.85 \times 10^{-12}$ F/m and α is the angle around the cylinder measured from the center of an electrode.

[28] Integrating the above equation over the area of electrode **0** gives the charge Q_{0x} induced on that electrode by E_{Sx},

$$Q_{0x} = 2\epsilon_0 E_{Sx} br2 \sin\psi \ , \tag{2}$$

where b is the length of the electrode along the axis of symmetry (z axis), r is the radius of the cylinder, and ψ is one half the angle subtended by the electrode. (In other words, the limits of integration for α are $-\psi$ and $+\psi$.) A similar result applies to the charge induced on electrode **1**, except for a minus sign that arises because the x axis of the coordinate system points away from this electrode instead of toward it,

$$Q_{1x} = -2\epsilon_0 E_{Sx} br2 \sin\psi \ . \tag{3}$$

[29] Induced charges on the electrodes are converted into voltages using charge amplifiers [*MacGorman and Rust*, 1998, p. 119]. The charge amplifiers are followed by voltage amplifiers with 10X gain (β = 10) that are also low-pass antialiasing filters. The frequency response of the circuits is 1 Hz to 5000 Hz; the edges of the band are defined to be the frequencies where the signal falls by 3 dB. Since the frequency response does not extend down to 0 Hz, the deduced values for charges will always be uncertain by

an additive constant. Since the total induced charges on the electrodes, and their corresponding voltages, are various linear combinations of the three components of the electric field and the net charge Q_I on the instrument, it is necessary to form linear combinations of the voltages to find the components of **E**. From symmetry, E_{Sy}, E_{Sz}, and Q_I contribute equally to the charges on electrodes **0** and **1**, and thus subtracting the voltages from these two electrodes will eliminate the effects of E_{Sy}, E_{Sz}, and Q_I. E_{Sx} is not eliminated because the expressions for Q_{1x} and Q_{0x} in the equations above differ by a minus sign. Similarly, since electrodes **2** and **3** are oriented along the y axis, subtracting **2** and **3** will eliminate E_{Sx}, E_{Sz}, and Q_I to leave only E_{Sy}.

[30] Putting all the pieces together gives an approximate expression for E_{Sx},

$$E_{Sx} = \frac{C(V_1 - V_0)/2}{4\epsilon_0\, \beta\, br \sin\psi} + E^0_{Sx}, \tag{4}$$

where C is the feedback capacitance in the charge amplifier circuit, and β is the voltage amplifier gain. E^0_{Sx} is an unknown constant that depends on the value of the electric field before a lightning flash begins. Thus the equation tells us the time-varying contribution of lightning to the electric field, but not the initial value before the lightning began. Equation (4) is approximate because it neglects the effects of the feedback resistance in the slow-antenna circuit. The approximation is valid for times much less than RC. For E fields varying on timescales somewhat greater than RC, the E field can be recovered by a more detailed analysis of the circuit, yielding a modified version of equation (4):

$$E_{Sx} = \frac{C\left(V^D_1(t) - V^D_0(t)\right)/2}{4\epsilon_0\, \beta\, br \sin\psi} + E^0_{Sx}\ , \tag{5}$$

where $V^D_1(t)$ and $V^D_0(t)$ are the "dedrooped" voltages at electrodes **1** and **0**, respectively. The measured voltage $V_1(t)$ is said to droop because a step change in the electric field at an electrode (electrode **1** in this example) will result in an output voltage that follows that step at first, then decays to zero with a time constant $R\ C$. The relation between the actual voltage and the dedrooped voltage is

$$V^D_1(t) = V_1(t) - V_1(0) + \frac{1}{RC}\int_0^t V_1(t')dt'\ . \tag{6}$$

The dedrooped voltages, V^D_0, V^D_1, V^D_2, and V^D_3, are useful because the electric field components are linear combinations of them plus an unknown constant. In our analysis we use the dedrooped voltages.

[31] It is useful to define w to be the width of the electrode before it is wrapped around the cylinder. With w defined this way, $\psi = w/(2r)$ radians and the area of the electrode is $A = bw$. Then we define

$$G = \frac{2\sin\psi}{\psi} \tag{7}$$

and

$$\Gamma = \frac{C}{\epsilon_0\, \beta A}\ . \tag{8}$$

With these definitions equation (5) can be rewritten as

$$E_{Sx} = \frac{\Gamma}{2G_x}\left[V^D_1 - V^D_0\right] + E^0_{Sx}. \tag{9}$$

While the expression for the y component is

$$E_{Sy} = \frac{\Gamma}{2G_y}\left[V^D_3 - V^D_2\right] + E^0_{Sy} \tag{10}$$

For our instrument, the width of the electrode is w = 0.09 m and the radius of the cylinder is r = 0.0762 m, and thus G = 1.88 given the approximation that the electrodes are not near the ends of the cylinder. In theory, G_x and G_y which appear in equations (9) and (10), are both equal to G of equation (7). Experimentally, these quantities are the instrument calibration factors Notice that $V_0\ \ldots\ V_3$ are measured voltages, while Γ is a simple multiplicative constant depending only on electrode area and physical constants. Thus we chose to lump all of our experimental uncertainty of the calibration of E versus V into G_x and G_y.

[32] The expression for the z component is

$$E_{Sz} = \frac{\Gamma}{4G_z}\left[\left(V^D_0 + V^D_1\right) - \left(V^D_2 + V^D_3\right)\right] + E^0_{Sz}\ . \tag{11}$$

Here G_z is the calibration factor for E_z versus V_n, analogous to G_x and G_y. Unlike G_x and G_y, an approximation to G_z cannot be derived analytically. However a simple thought experiment will illustrate how we know the form of equation (11) is correct.

[33] If one imagines a purely vertical upward field E_{Sz}, one sees that the lines are distorted near the Esonde and must bend to enter the surface of the cylinder at a right angle. The cylindrical symmetry of the Esonde causes the number of field lines entering at electrode **0** at the bottom of the sonde to be the same as the number entering at **1**. Identical charges are induced, so $V_0 = V_1$ in this imaginary pure z field. As the Esonde and the electrode placement is symmetrical about the Esonde midpoint, the same number of lines that enter at electrode **0** and **1** should leave at electrodes **2** and **3** at the top of the sonde. This electrical thought experiment justifies the use of a weighting factor of equal magnitude for each electrode in a z axis field, with a sign flip for the upper two, just as shown in equation (11).

[34] To find G_z and to check the validity of the approximation that $G_x = G_y = 1.88$, we calibrated the balloon-borne Esonde in a stand near the ground by comparison with an existing ground-based field mill (Figure 4). The calibration stand holds the Esonde at a roughly 45° angle to the ground so that the three components E_{Sx}, E_{Sy}, and E_{Sz} are nonzero and have a known relationship to **E**, which is directed perpendicular to the ground. The result of this calibration is that G_z = 2.4 ± 0.3 and $G_x = G_y$ = 2.7 ± 0.4. It is unsurprising to find G_x and G_y are larger than the theoretical values, for our cylinder is not infinite. The instrument parameters needed to find Γ, the other constant in equations (9)–(11), are C = 22 nF, β = 10, A = 0.01 m^2, and $\epsilon_0 = 8.86 \times 10^{-12}$ F/m. With these values, Γ = 24,800 m^{-1}.

[35] It is reasonable to assume on the basis of the symmetry of the instrument that $G_x = G_y$, and this assump-

Figure 4. The Esonde calibration stand is made of a dielectric material which holds the Esonde 2 m above the ground with the vertical axis inclined by roughly 45°.

tion carries into our experimental calibration procedure. The ''rainhat'' or hood mounted on top of the Esonde somewhat breaks the symmetry by slightly overlapping the y axis electrode. The hood is made from a 1-mm thick polypropylene salad bowl with relative permeability $\epsilon_R \simeq 2.1$. While this is sufficient to create a nontrivial polarization surface charge in the presence of an external E field, all field lines that terminate on the outer surface of the bowl should reappear on the inner surface. While it may develop bound charge, the hood should not significantly affect the field change produced by lightning at electrodes **2** and **3**. The calibration procedure described is not a laboratory procedure, but requires the instrument to be put out in a storm. In the future, multiple instruments with differing orientations could measure G_x and G_y individually rather than together. This would provide a rigorous test of our assertion that $G_x = G_y$.

[36] In further analysis of the data, we used the experimentally determined values for $G_x = G_y = 2.7$, rather than the infinite-cylinder value $G_x = 1.88$. For G_z, there is no simple analytical solution; the experimental value $G_z = 2.4$ was used in further analysis.

2.6. *E* Field Components in an Earth Reference Frame

[37] The components of **E** derived using the method outlined above are in a reference frame that moves with the instrument. To compare the time variation of **E** with the locations of lightning channels, it is necessary to transform the components of **E** to a reference frame fixed with the Earth; we call these components ''Earth-referenced'' in our figures, and define them in Table 2. We will be very specific about our conventions, but in a nutshell, our coordinate conventions are those common in physics, rather than those common in cartography. We define the positive direction for E_x to be due east, the positive direction for E_y to be true north, and positive E_z is up, away from the Earth.

[38] Unfortunately, the three components of the Earth's magnetic field **B**, measured by the magnetometer in the coordinate system fixed with the instrument, are not sufficient to determine the orientation of the instrument relative to Earth. This problem can be visualized by imagining the instrument to be rotated about an axis parallel to the direction of the Earth's magnetic field. During such a rotation, all components of **B** measured by the magnetometer will stay the same.

[39] The problem can be adequately solved by reducing the amount the instrument swings beneath the balloon. We do this with a damper that produces drag in the air as the balloon swings. The damper is made from two sheets of nylon 1.3 m tall by 0.8 m wide that intersect each other along a vertical line. From the top, the damper looks like a plus sign so that it will produce drag during swinging in any direction. A side view of the damper is visible in Figure 5 (item F). The magnitude of the swinging can be inferred from the angle θ_B, the angle between the instrument's z axis and the direction of the Earth's B field.

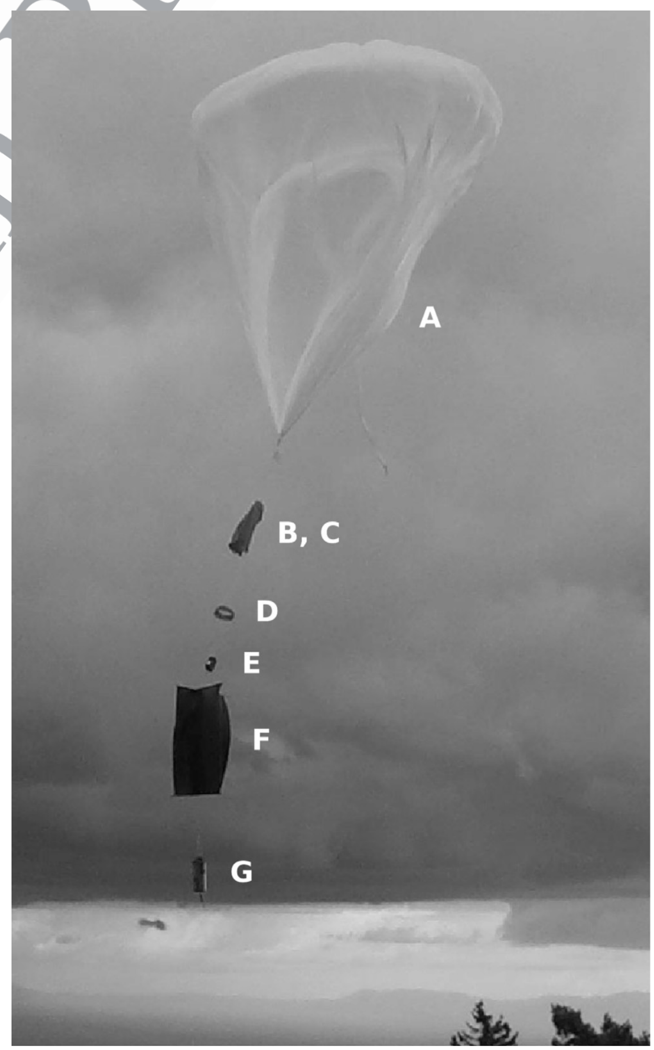

Figure 5. The balloon train is shown, including, from top to bottom, polyethylene balloon, indicated by A; 1.6-m diameter nylon parachute, indicated by B; balloon cut-down package hidden inside parachute, indicated by C; antitangle ring, indicated by D; auxiliary tracking package, indicated by E; nylon damper, indicated by F; and Esonde, indicated by G.

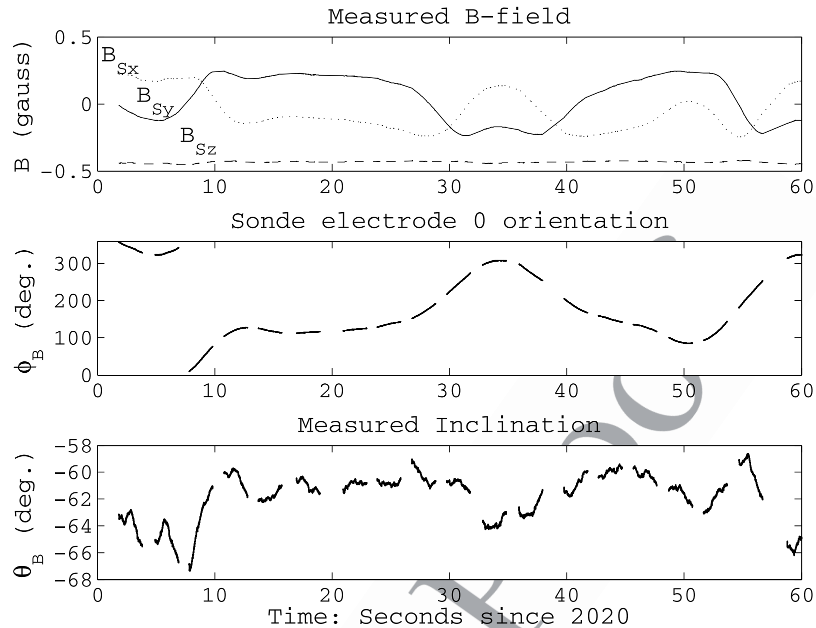

Figure 6. Earth's field is measured to determine instrument orientation. (top) Shown are components of **B** for the minute that includes the CG flash. (middle) Shown is rotation angle ϕ_B defined as the positive counterclockwise angle from the Esonde x axis to the direction of the Earth's B field. The Esonde makes approximately one full revolution. (bottom) The measured inclination θ_B suggests that the Esonde deviates from vertical by ±4°. Figures 6 (middle) and 6 (bottom) show breaks in the data. As previously discussed, these occur while data are being written to flash memory. The somewhat longer breaks at roughly 20, 40, and 60 s into the minute occur when the 8 "slow" data channels are checked and all the data are telemetered to ground. The data in Figure 6 (top) also have gaps, but smooth lines span them.

[40] We call the quantity θ_B the "measured inclination," and calculate it as follows,

$$\theta_B = \arcsin\left(\frac{B_{Sz}}{B}\right), \tag{12}$$

where B is the total magnitude of the Earth's field measured by the Esonde. For the case when the instrument axis is perfectly vertical, the measured inclination (θ_B) is the same as the actual inclination (θ_I), as conventionally defined in magnetic navigation.

[41] At times when the instrument is swinging toward or away from the direction of the Earth's magnetic field, θ_B will show the greatest deviation away from 61.3°, which is the magnetic inclination in the vicinity of Langmuir Laboratory. Figure 6 (bottom) shows typical variations in θ_B for a time interval of 1 min, when θ_B varies between 60° and 68°.

[42] With swinging reduced so that the z axis of the instrument is nearly vertical, B_{Sx} and B_{Sy} can easily be used to find the orientation of the instrument x axis (electrode **0**) with respect to an Earth-referenced x axis (true east). The Esonde is assembled such that the center of electrode plate **0** is aligned with the x sensor direction of the magnetometer, while plate **2** is aligned with the y sensor. Consider the Esonde to be held vertically and turned such that B_{Sy} is a maximum positive value, while B_{Sx} is roughly zero, i.e., electrode **2** is toward magnetic north. With the Esonde in this orientation, if a lightning flash occurs causing E_{Sx} as defined in equation (9) to be positive, the **E** vector would be pointing magnetic east. Likewise, a flash resulting in positive E_{Sy} corresponds to a magnetic northward E field.

[43] The orientation angle ϕ_T of the Esonde is determined by

$$\phi_T = \phi_B + \phi_D = \arctan\left(\frac{B_{Sy}}{B_{Sx}}\right) + \phi_D, \tag{13}$$

where ϕ_T is the angle between electrode **0** and true north, ϕ_B is with respect to magnetic north, and ϕ_D is the declination angle (+10.0°). All angles in the $x-y$ plane of the Esonde are defined counterclockwise positive from the x axis. The quadrant in which the arctan is placed must be determined by the signs of B_{Sx} and B_{Sy}.

[44] Figures 6 (top) and 6 (middle) show the components of **B** and the calculated ϕ_B, respectively. The Esonde appears to be rotating at instantaneous rates of up to 5 rpm.

[45] Having outlined the way in which Earth-referenced E field data can be recovered, we proceed to real data to further illustrate the analysis process and see what can be learned about lightning.

3. Cloud-to-Ground Flash, 2020:21 UT

3.1. Results

[46] Figure 7 shows radio frequency sources from lightning detected by the LMA for a multistroke CG flash that occurred on 18 August 2004, at 2020:21 UT. The O indicates the position of balloon and Esonde at time of flash. The flash begins near the X and advances to the

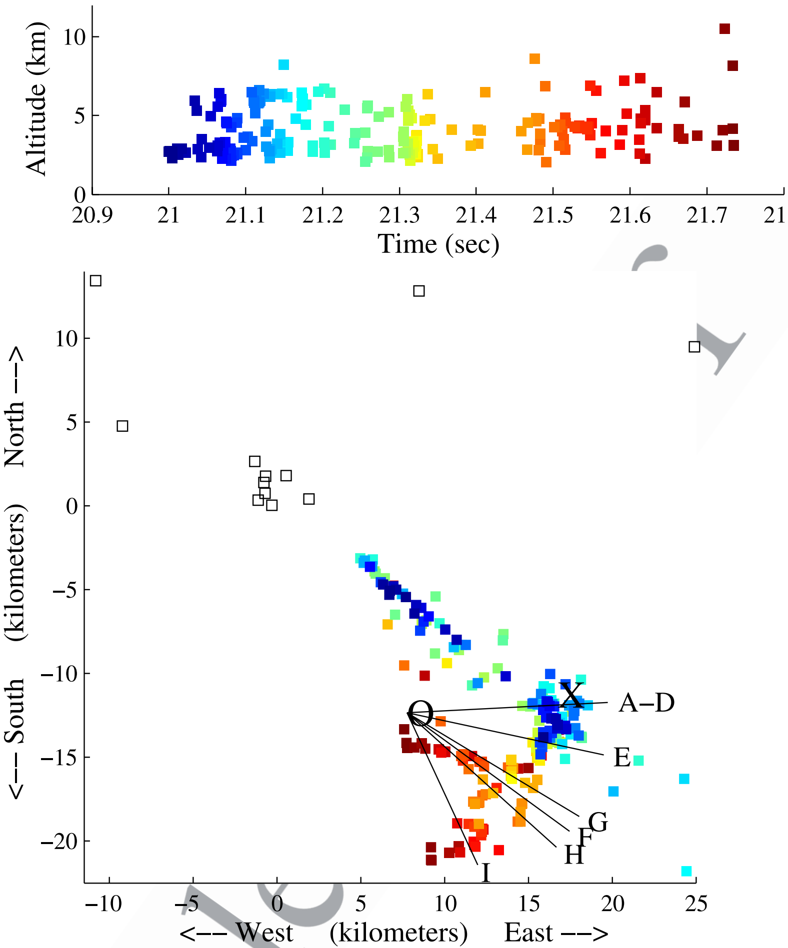

Figure 7. Shown are sources of radio frequency (RF) pulses from the LMA and directions of electric vectors indicated by the balloon-borne Esonde for the flash at 2020:21 UT. The O indicates the position of balloon and Esonde at time of flash. The X is the location (by NLDN) of the CG strokes. Open black squares are locations of LMA base stations, while solid colored squares are RF source locations. Color indicates the passage of time in both panels of the figure. The top plot allows time to be assigned to colors in the bottom plot with some precision. The flash begins near the X and advances to the southwest. The radial lines originating at the balloon are vectors to the detected charge centroids for each of the labeled strokes. The angles of these lines are reported in column 10 of Table 3.

southwest. The origin of the coordinate system is at Langmuir Laboratory in the Magdalena Mountains of New Mexico (latitude 33.9752°N and longitude 107.1811°W).

[47] The open black squares on the plot represent the positions of the LMA receivers. Most of the receivers are in a compact array configuration around Langmuir Lab to increase sensitivity immediately over the Lab. The 2020:21 UT flash is outside the optimum area for the array. Note that a number of the blue data points (corresponding to early times during the flash) make a line pointing toward the origin of the coordinate system. This is a known LMA artifact when there is radial range misdetection, informally called "spoking error" [*Thomas et al.*, 2004]. The LMA receivers clustered at Langmuir Lab are almost in a line with the spoke. As the flash propagates southwest, the colinearity of the stations at Langmuir Lab is sufficiently broken that the range detection improves and the two major branches of the lightning channel (orange and red points) are relatively clearly resolved. The three widely separated outlying receivers also help, though some of them are likely not detecting the lightning because of intervening mountains.

[48] Having accounted for the spoking error, we can say that the LMA shows that the initiation point for the flash is actually in the cluster of points around the X, which is roughly 12 km south and 17 km east of the Laboratory. The flash then propagates southwest and branches into two major channels.

[49] Ground-strike points determined by the National Lightning Detection Network (NLDN) show seven negative CG strokes occurring over a ±2 km region centered on the X. Table 3 gives the NLDN coordinates for these CG strokes in columns 3 and 4. On the basis of the typical location error for the modern NLDN [*Idone et al.*, 1998; *Cramer et al.*, 2001], it appears there are one or two distinct channels to ground shared by all the strokes.

[50] Figure 8 shows the voltages from the charge amplifiers for each electrode and the GPS pulse that occurs precisely at the beginning of each second. As was shown

Table 3. Location of Stroke Charge Centers Compared Between National Lightning Detection Network and Esonde[a]

	National Lightning Detection Network						Esonde					
Stroke	Time, s	Latitude	Longitude	Δy, km	Δx, km	ϕ	ΔE_x, V/m	ΔE_y, V/m	ϕ	ΔE_z, V/m	Q_{min}, C	Q_{max}, C
A	21.023	33.877°	−106.991°	−11.16	17.56	7.0°	−100	10	6°	−290	3.5	7.
B	21.043	33.874°	−106.99°	−11.27	17.65	6.3°	−40	3	4°	−105	1.3	2.5
C	21.102	33.869°	−107.01°	−11.83	15.80	3.8°	−100	5	3°	−290	3.5	7.
D	21.13						−65	5	4°	−145	1.8	3.5
E	21.316	33.88°	−107.013°	−10.60	15.52	12.7°	−95	20	−12°	−230	2.	4.
F	21.34						−600	430	−36°	−1250	5.	15
G	21.549	33.948°	−106.995°	−3.03	17.19	44.6°	−30	18	−31°	−50	0.2	0.6
H	21.613	33.875°	−107.006°	−11.15	16.17	8.1°	−230	240	−46°	−510	2.	6.
I	21.690	33.875°	−107.011°	−11.16	15.71	8.6	−75	165	−65°	−270	0.5	3.
Balloon	21.	33.864°	−107.097°	−12.36	7.75					Q_{total}	22	49

[a]The left side of the table (columns 2–7) shows NLDN data, or values derived from NLDN data. The NLDN is operated for the United States by Vaisala Corporation. The right side of the table (columns 8–13) reports measurements by the Esonde for the same strokes. Strokes D and F were seen by the Esonde but not reported by NLDN. Ground strike latitude and longitude (columns 3–4) are obtained from NLDN. Columns 5 and 6 report distance in km from origin at Langmuir Lab to NLDN points. ϕ data in column 7 are obtained trivially from columns 5–6 and known coordinates of balloon. One can compare the angle reported in column 7 with the angle obtained from Esonde data reported in column 10. **E** data for each stroke are measured by our instrument. ΔE_x and ΔE_y (columns 8–9) are used to calculate ϕ (column 10). If $\phi = 0°$ the charge center is located due east of the balloon. ΔE_z (and parameters explained in the body of paper) are used to calculate the magnitude of Q (columns 12–13). Uncertainty in Q is greater for points F–I as a second branch of the lightning channel increases the range of distances from which charge may be drained. The estimated total charge brought to ground by this flash is −22 to −49 C. The position of the balloon at the time of this flash is listed on the final row of the table.

in Figure 1, electrode **1** is at the bottom and electrode **3** is at the top of the Esonde cylinder. Note that the waveforms V_1 and V_3 in Figure 8 are approximate mirror images of each other. For E field changes with large vertical components, this approximate mirror image response is expected from elementary electrostatics, as explained earlier in the discussion of equation (11). The reason the wave forms are not exact mirror images is that electrodes **1** and **3** are facing in different horizontal directions, and the field changes have horizontal as well as vertical components.

[51] The dotted line in Figure 8, showing a square pulse with leading edge at precisely 21.000 s, is the digitized pulse-per-second output from the GPS. The pulse-per-second line is connected to the A/D converter so that its data are interleaved with the voltages from the electrodes and the magnetometer. In analyses of over 20 flashes, with this method of timing, it was found that lightning features observed in the Esonde data coincide with the same events in LMA and NLDN data without any offsets applied to timing. This supports our earlier statement that $Err_t^{ES} \simeq 20\ \mu$s.

[52] In Figure 9 the sums and differences and calibration factors indicated in equations (9)–(11) have been applied to the voltages from individual electrodes. These components are called "sonde-referenced" because the x, y, and z axes are attached to the Esonde. The data have also been corrected (dedrooped) to compensate for the effect of the feedback resistor in the charge amplifier.

[53] Figure 10 shows **E** in Earth-referenced coordinates in which the x axis is east, the y axis north, and the z axis up.

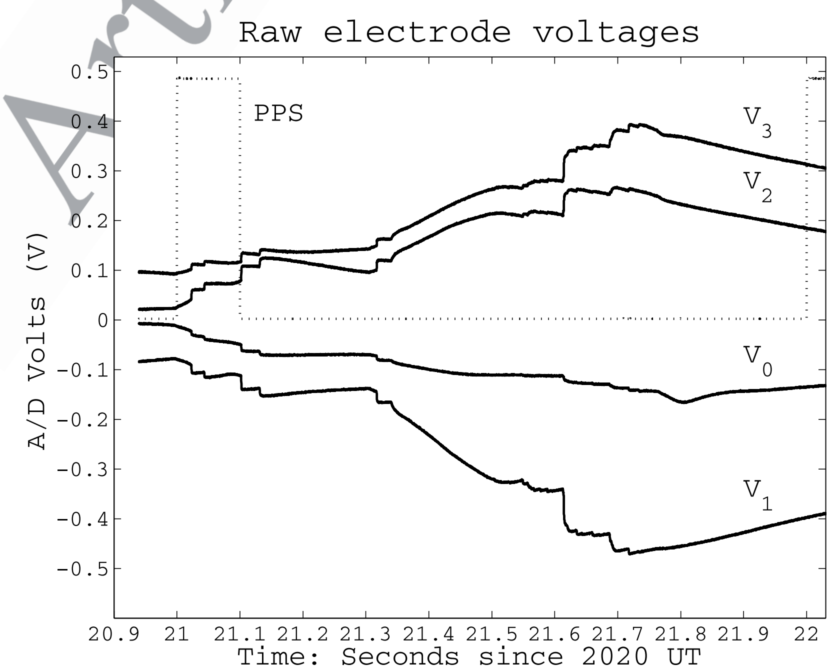

Figure 8. For the CG flash at 2020:21 UT, the figure shows the voltages from the charge amplifiers for each electrode and the GPS pulse that occurs precisely at the beginning of each second.

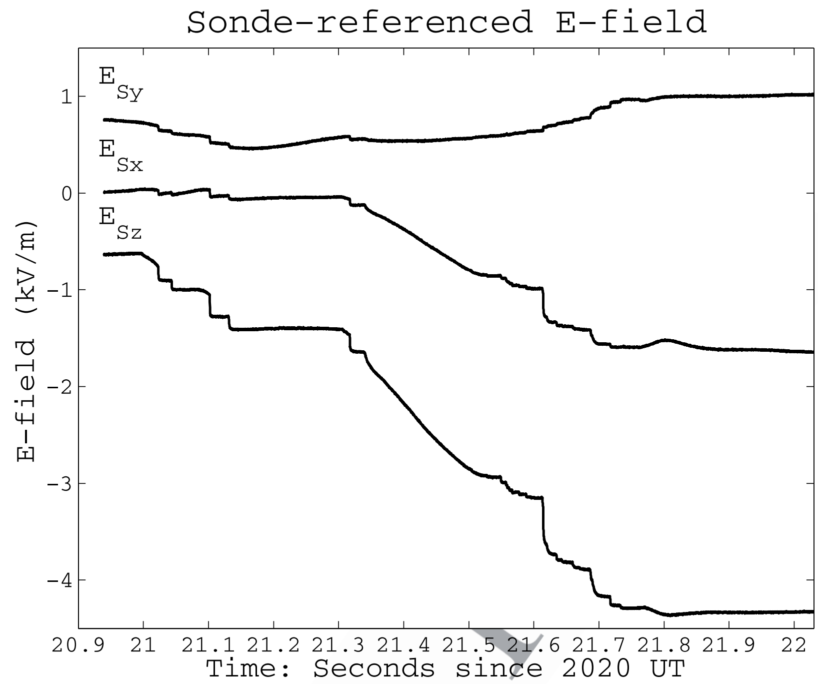

Figure 9. Components of **E** in the Esonde coordinate frame are shown. The vertical placement of each curve is arbitrary, since each curve has an unknown additive constant, as previously described.

Each CG return stroke is labeled with a letter. These are the same letters used in Table 3. A long continuing current can be seen after stroke F, and stepped leaders are evident before the return strokes of A and E. From these data, ΔE_x, ΔE_y, and ΔE_z are derived, and they are reported in columns 8, 9 and 11 of Table 3.

[54] The components of $\Delta\mathbf{E}$ are derived by measuring the *E* field steps labeled in Figure 10. We use the same technique as *Krehbiel et al.* [1979], which is illustrated in Figure 11 for step E. Though the steps in Figure 10 appear rather small, Figure 11 shows that the signal-to-noise ratio of the data is more than adequate to measure the step heights to a little better than two significant figures.

[55] The dominant uncertainty in our absolute measurements then is the uncertainty in the instrument calibration previously discussed. By symmetry, we can assume that the

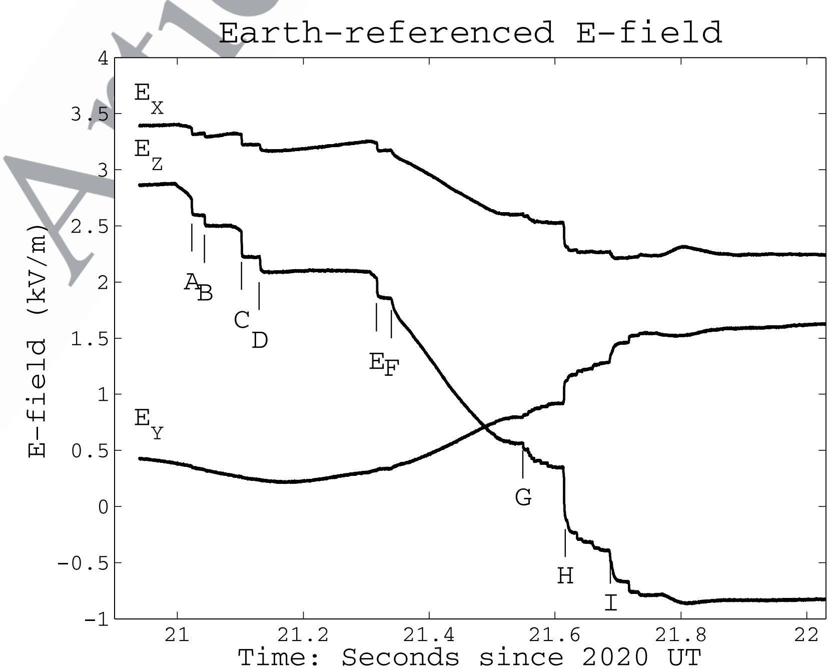

Figure 10. A rotation using ϕ_T was applied to the Figure 9 data to produce the Earth-referenced fields shown here. If E_x is positive, the field vector is pointing east. If E_z is positive, the field vector points up. Each step in **E** is labeled to correspond with the entries in Table 3. The vertical line below each lettered step is set at exactly the time listed in column 2 of Table 3.

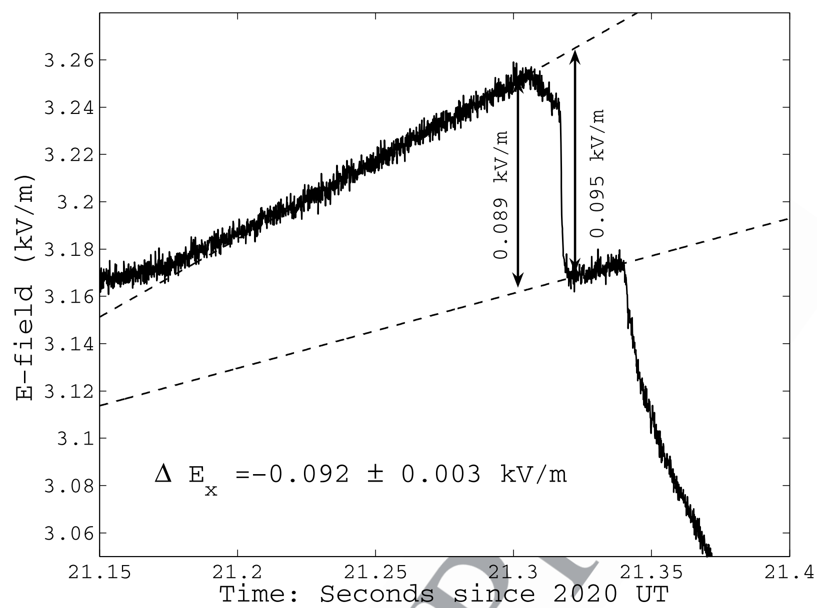

Figure 11. Shown is the fitting process yielding a step in **E** caused by CG lightning. The distance between baselines is measured before and after the step and is averaged. This is stroke E in Figure 10 and Table 3. Note the stepped leader preceding this CG stroke. These data also show the baseline noise of our instrument to be about 3 V_{RMS}/m.

relative calibrations in $x - y$ plane are equal, so for certain calculations we can use the full precision of our data. For calculations in which the relative $x - z$ strength is important, or in which the absolute value of E field matters, we are limited to the single significant figure of our instrument calibration. With these caveats, the measured $\Delta\mathbf{E}$ components are used in all subsequent data analysis of the CG flash.

3.2. Horizontal Location of Charge Centroid

[56] To analyze the location of the charge centroid of a lightning stroke, one needs only to assume that a CG stroke serves to discharge a section of cloud. The simplest physical model is a point charge at a location in the cloud, an image charge of this point charge in the ground below, and the neutralization of both by the stroke. As published cloud charge densities ρ are typically of order ρ = 1 C/km^3 [*Marshall and Rust*, 1991], one must understand the "point-charge" assumption to be an approximation in which the position is not a point, but rather the location of the centroid of charge neutralized in the stroke. With this simple model, the field changes ΔE_x and ΔE_y reported in columns 8 and 9 of Table 3 can be used to calculate a direction angle to the centroid. Equation (14) gives the angle ϕ to the charge centroid with a coordinate origin at the Esonde.

$$\phi = \arctan(\Delta E_y / \Delta E_x), \tag{14}$$

[57] The results of equation (14) are in column 10 of Table 3, and a line with this same angle labeled with the letter of the flash is overlaid onto Figure 7.

[58] For comparison, columns 3 and 4 of Table 3 show latitude and longitude of ground strikes obtained from the NLDN. Columns 5 and 6 display distance of these NLDN strike points from the coordinate origin at Langmuir Lab. For all but stroke G, the NLDN locations cluster around coordinates (x = 17, y = −11) km. For convenience, an X is placed at these coordinates in Figure 7. The angle ϕ to the centroid may also be calculated using the known Esonde coordinates and the reported NLDN coordinates from columns 3–4. This alternate value of ϕ is reported in column 7 of Table 3. Columns 7 and 10 agree well for strokes A–D, but differ increasingly for strokes E–I.

[59] The apparent disagreement in ϕ for strokes E–I admits a physical interpretation. The ground strike points, reported by the NLDN, are identical within the location error of the NLDN, or perhaps represent two channels to ground about 1 km apart. (Only stroke G appears at a very different location, a location with no LMA points at all. Thus this is a mislocation by the NLDN caused by a rather small CG discharge.) In contrast, the column 10 angles represent the directions to the charge centroids. There is no reason why the charge centroid should remain above the ground strike points. We interpret the result as a clear demonstration that the portion of the cloud being discharged grows increasingly distant from the ground strike points as the flash proceeds. In Figure 7, it appears that the southwestward motion of the charge center being drained is consistent with the growth of the ramified branches shown by the LMA points.

[60] For reference, in a summer Florida storm, *Uman et al.* [1978] reported a single flash transporting −47 C to ground in three large strokes with ΔQ = −25, −14 and −8 C respectively. Our finding that the direction to the charge center moves steadily away from the ground-strike point is similar to their report that the charge centers were displaced horizontally away from the main return stroke channel with increasing stroke order.

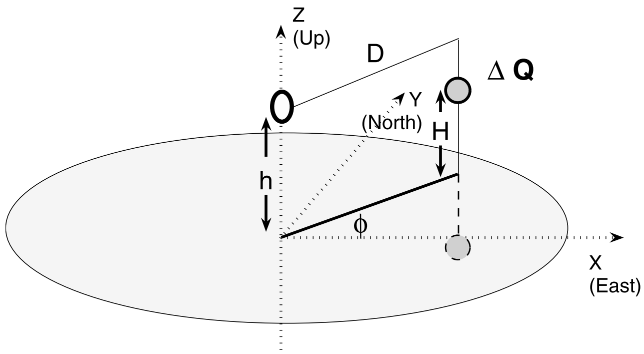

Figure 12. This sketch illustrates parameters in equation (15). The large ellipse represents the ground. The egg-shaped oval a distance h above ground is the balloon and Esonde. A cloud charge ΔQ is a distance H above ground, and its image charge is equidistant below ground level. This sketch shows the case of flat terrain at sea level. For the ground at elevation e, an additional term is included in equation (15), because the image charge altitude is changed by $2 \times e$ relative to sea level.

3.3. Charge Transferred for Each Stroke

[61] Coulomb's law can be used to estimate the charge ΔQ transferred to ground by each stroke in the 2020:21 UT flash. The charge is calculated from the following equation.

$$E_z = \frac{1}{4\pi\epsilon_0}\left\{\frac{\Delta Q(h-H)}{\left[D^2+(h-H)^2\right]^{3/2}} - \frac{\Delta Q(h+H-2e)}{\left[D^2+(h+H-2e)^2\right]^{3/2}}\right\} \tag{15}$$

[62] Figure 12 illustrates the quantities in the above equation. ΔQ is the total charge transferred by the CG flash; h is the altitude of the Esonde as measured by the GPS; H is the altitude of the charge center neutralized. Figure 12 and equation (15) also show an "image charge" of magnitude $-\Delta Q$ below the plane of the ground. Though h and H are expressed relative to sea level, the balloon is flying over mountainous terrain. Therefore e, the elevation of the terrain directly under the flash, is also included in equation (15). For simplicity, the dimension e is not shown in Figure 12.

[63] In calculating the charge for strokes A–D, the lateral distance D from balloon to a stroke is taken to be 9. ± 1. km. This value was chosen because it is the distance from the Esonde to a high concentration of RF source points (shown in Figure 7) at the time when the flash begins. The high concentration of LMA points also overlaps the region, marked by an X, in which NLDN ground strikes were observed. The balloon altitude h at 2020 UT is known from GPS to be 3.0 km. The elevation of the ground e at the latitude and longitude of the flash is estimated to be 1.8 km from topographic maps. Local topographic maps also support the approximation that the area is a plateau, rather than a mountain, and thus that the ground is a plane. The height of the centroid of charge transferred to ground H can also be estimated by assuming that it comes from the middle of the negative charge center outlined by the LMA data in Figure 7 (top). For this flash, the LMA data have rather broad altitude distribution. Our best estimate is that the charge originates at altitude H = 5. ± 1. km. Minimum and maximum values of charge calculated from these assumptions are presented in Table 3, columns 12 and 13. Charge transferred to ground ranges from −1.3 to −7. C for strokes A–D.

[64] For strokes E–I, the same formula and range of H can be used to calculate the likely charge transferred. However, since we claim that the NLDN does not measure the charge centroid for these later strokes, we extrapolate for distance D on the basis of the LMA locations and the angles ϕ listed in column 10 and discussed in the previous section.

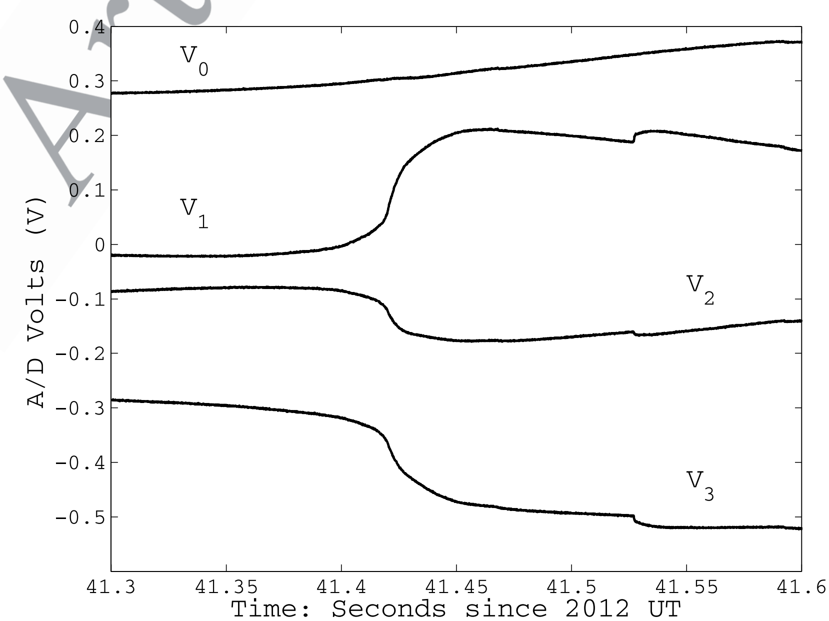

Figure 13. Shown are voltages from the charge amplifiers for each electrode at the time of an IC flash. The offsets of V_0–V_3 were chosen for clarity of the figure. Recall that DC levels of these voltages are set to zero immediately before a flash.

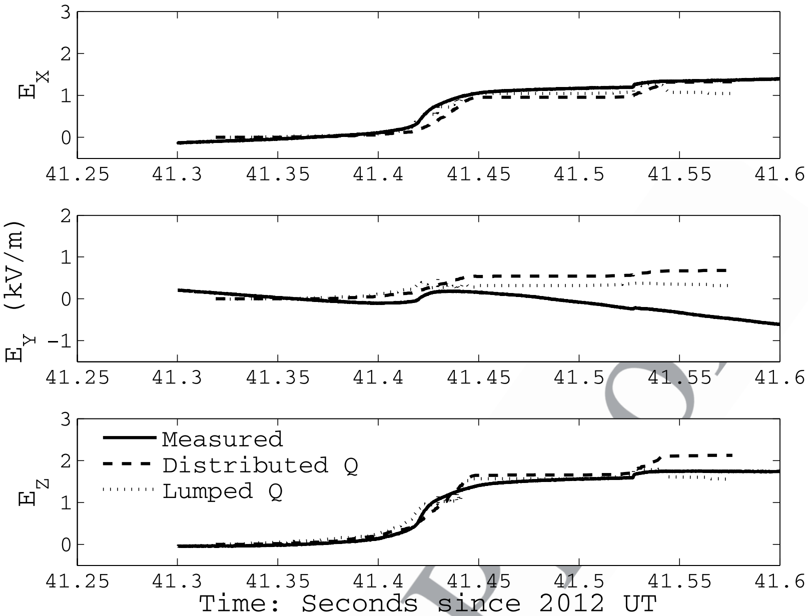

Figure 14. Measured Earth-referenced fields, E_x, E_y, and E_z (solid lines) are compared with two simple models derived from LMA data for the flash. The dashed line is obtained by distributing a total charge of −23 C evenly among the LMA points as the flash progresses. The dotted line and the step at 41.42 s are obtained by putting −4 C at the end of the lightning channel and moving it along with the channel. The smaller step at 41.53 s is obtained by putting an additional −1 C at the end of the channel. The smaller step is caused by the 2nd surge of charge referred to in Figure 15.

For stroke E the uncertainty in distance D is not larger than it was for strokes A–D. For strokes F–I, the lightning channel is seen to branch. One branch maintains approximately a 9-km distance from the balloon, but the other branch gets much closer. Depending on our assumption of how the charge is drawn from the two branches, we calculate very different charges transferred. The data in column 13 for stroke E assume $D = 8. \pm 1$ km. For strokes F–H, we assume $D = 6. \pm 2$ km. Stroke I is the most ambiguous. We can say only that D ranges between 2 and 8 km.

[65] Examination of Figure 10 shows a barely visible stroke (F) with a large continuing current. Both the stroke and the continuing current were counted in the calculation of charge transferred for Table 3. It is interesting to note that the NLDN did not report this stroke despite the large charge transfer. Stroke H has the largest ΔE_z at the return stroke. The total charge transferred by the flash for strokes A–I is −22 to −49 C, depending on the assumptions concerning charge height H and distance D.

[66] This flash, with a multiplicity of at least 9 strokes, gave individual stroke results typical of *Krehbiel et al.* [1979], who reported, in New Mexico storms, on four flashes with multiplicities of 5 to 7 with a total charge transferred ranging from −30 to −66 C. The individual strokes in the flashes reported by Krehbiel et al. transferred between −1 and −21 C. Thirteen of these strokes transferred a negative charge with magnitude <4 C. This is in better agreement with our results of Table 3 than the −8 to −25 C reported by *Uman et al.* [1978], which we mentioned earlier.

[67] We also used E_x and E_y measurements, with a similar approach, to calculate the ΔQ values. The ΔQ obtained in this way disagreed by as much as 20% from the ΔQ obtained from E_z. The discrepancy is caused by the approximation that all of the charge brought to ground originates at a point. One expects the charge area drained to be an extended horizontal region, a fact recognized by *Few and Teer* [1974]. The error that a horizontally extended charge adds to the calculations is different for E_x and E_z. Because E_z is less sensitive to horizontal extent of ΔQ than is E_x, use of E_z gives a more robust method of calculating the magnitude of ΔQ, precisely because it is relatively insensitive to its horizontal distribution.

4. Intracloud Flash, 2012:41 UT

[68] The above analysis of a CG flash was based on the presence of a number of abrupt changes in the electric field. During the IC flash under consideration in this section, the electric field was generally smooth with more gradual changes; thus the analysis proceeds differently.

4.1. Results

[69] Figure 13 presents the voltages measured by the Esonde for each electrode. From these voltages, components E_x, E_y, and E_z are calculated by the same procedure used for the CG flash. Figure 14 presents these components, represented by solid lines. The dotted and dashed lines are the results of modeling, which will be discussed in the next section.

[70] Figure 15 shows sources of RF radiation from lightning channels during this flash.

[71] The initial breakdown is first visible at 2012:41.32 UT with a negative streamer moving into the upper positive charge center. This interpretation is supported by the observation that negative streamers propagating into a positively charged region are more highly impulsive and radiate more

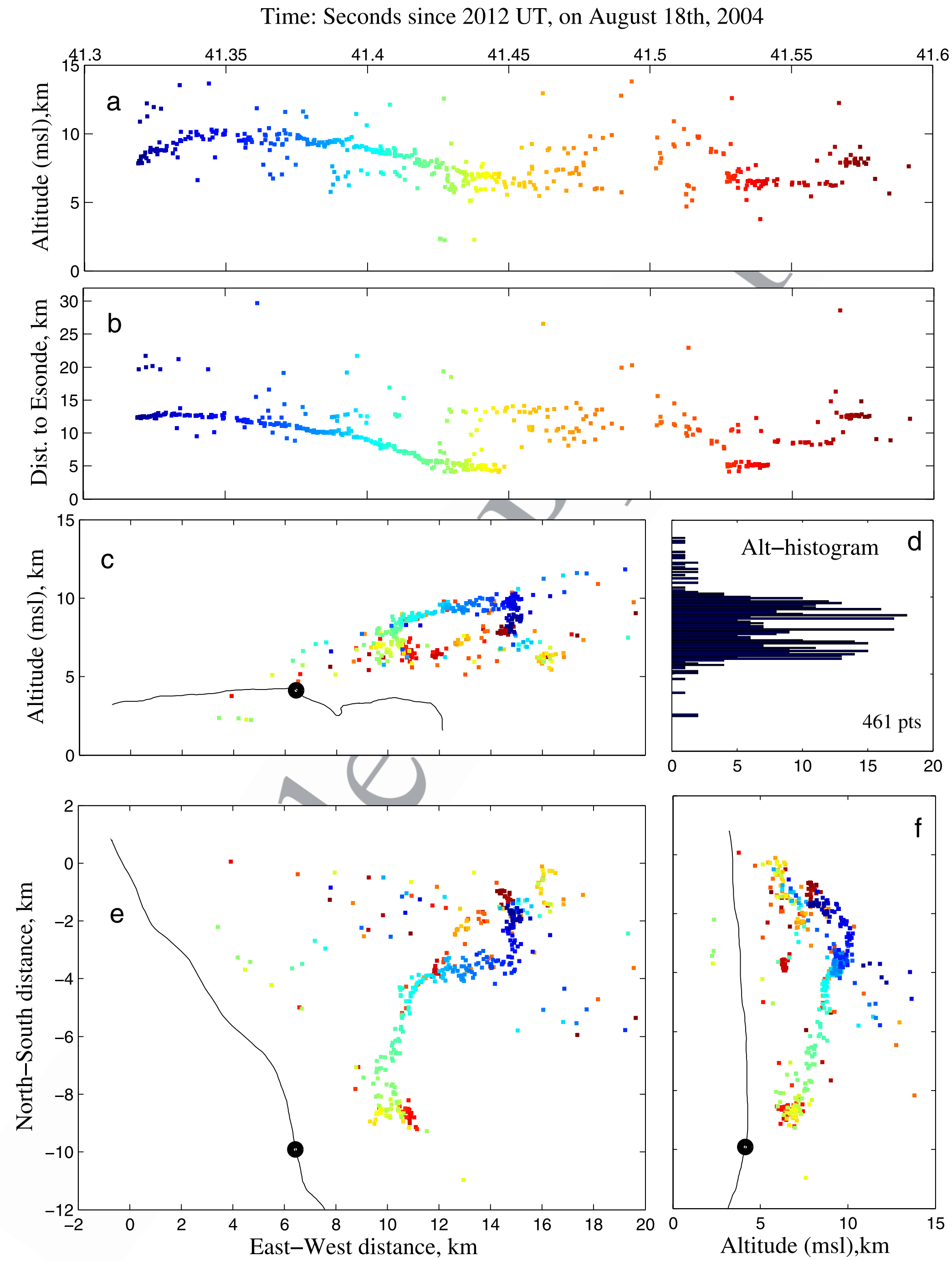

Figure 15. Shown are LMA sources for an IC flash at 2012:41 UT and the balloon track for roughly 30 min surrounding this time. (a) This plot shows altitude versus time and also defines the color versus time scale used for Figures 15b–15f. The upward initiation of the channel points to a negative IC leader in a normal polarity storm. (b) Shown is distance from LMA points to the balloon versus time. A major channel is seen to approach the balloon beginning at 41.32 s. Then, at around 41.5 s, a second surge of charge approaches along the same channel. (c) The solid dark line is the balloon track. At the time of the flash, the balloon is at the position indicated by the large black dot. (d) The source histogram points out the bilevel charge structure of the cloud. The lower negative charge is at 6 km, and the upper positive charge is at 9 km. (e) The plan view also shows the balloon track. The lightning channel clearly approaches the balloon from the north and east. (f) This plot most clearly shows that the channel descends on the balloon but remains above at all times. The IC flash at 2012:41 UT was not detectable by the NLDN.

power than positive streamers propagating into a negatively charged region [*Rison et al.*, 1999]. Furthermore, coordinated observations using the LMA and balloon-borne electric field meters show that an upward moving initial breakdown (evident in Figure 15a) occurs between an upper positive charge and a lower negative charge in a normal polarity storm [*Coleman et al.*, 2003]. Beginning with this insight, it is reasonable to conceive of the IC flash as transporting net negative charge toward the Esonde from 2012:41.32 until 2012:41.45 UT. Negative charge arriving northeast of the Esonde should result in the north (E_y) and east (E_x) components of **E** growing more positive, exactly what Figure 14 shows. Further, the LMA sources in Figure 15 clearly show that the channel propagates above the Esonde and descends from 10 km to 6 km altitude toward it. The approach of negative charge from above suggested by the LMA data ought to result in an increase in E_z, and this is also what Figure 14 shows.

4.2. Model

[72] Having argued a qualitative interpretation of the data, we try two simple models to make it quantitative and see what else can be learned by combining E field with LMA data. For both models, we assign a charge δq at the coordinates of each LMA noise point. The value of δq, and how it varies in time, is different for the different models.

4.2.1. Lumped Charge Model

[73] In the first model, the "lumped charge" model, the charge δq is a point charge at the tip of the channel and contains all the charge that a given channel of a flash is going to carry. At the time that the channel originates, equal and opposite charges δq and $-\delta q$ are placed on the first LMA source point. When the next LMA noise source emits, the charge δq is moved to the coordinates of the new emission, while $-\delta q$ remains at the channel origin. This continues until it appears from the LMA plot that the leader channel has reached its end. When that occurs, the charge δq is left at the end of the channel. The charge $-\delta q$ left at the channel origination point serves to conserve charge. When the next leader starts up, a (possibly different) δq and $-\delta q$ are applied at its initial point, and the new δq moves until the leader terminates.

[74] A charge $\delta q = -4.0$ C is moved along from one LMA point to the next between 41.32 s and 41.45 s. Figure 15b shows that the lightning channel makes a closest approach to the Esonde of about 3 km at 41.45 s. The points immediately after 41.45 s are substantially further from the Esonde. The point at 41.45 s is considered to be the terminus of the first leader channel, and so -4.0 C is left at this location. Beginning immediately after 41.450 s, a new leader moves up the previously existing channel, this time with $\delta q = -1.0$ C. This charge is allowed to propagate with the developing leader, and results in a step in field at 41.53 s, as the red LMA points are approaching the Esonde. This smaller charge is then left at the end of the channel at 41.55 s.

[75] Charge conservation was applied by assuming that there was a +4 C charge left at the location of the blue data points at 41.32 s. It did not move once it was placed. Beginning at 41.45 s, an additional +1.0 C was placed at the location of the light orange LMA points.

[76] The modeled E field in the lumped charge model was calculated in a rather obvious, if brute force, way. For E_z equation (15) was used, with the variables defined as they were for the CG flash discussed in the last section. The value of D was calculated from the known position of the Esonde and the coordinates of the appropriate LMA noise point. (The LMA data for this flash are more dense than for the CG flash, making the analysis more precise). H was also obtained from the LMA data point at the corresponding instant of time. For simplicity the elevation e of the ground above sea level was assumed fixed at 1.9 km. The altitude h of the balloon was known from GPS to be 4.1 km MSL. A similar procedure was used for the calculation of E_x and E_y with only adjustments to the trigonometry of equation (15) (which is after all only Coulomb's Law with the inclusion of an image charge).

[77] The results of the lumped charge model are shown as dotted plots and compared against all three E field components in Figure 14. These two values of δq were selected on the basis of a simple eyeball fitting of the model to the experimental data. Note that both values somewhat overestimate the change seen in E_z, and underestimate the change in E_x. While this points out that our model is inadequate, it is fair agreement considering the simplicity of the assumptions.

4.2.2. Distributed Charge Model

[78] The second model uses a distributed charge. For the first point of a branch, this model begins like the lumped charge model. A charge δq is placed at the coordinates of the initial noise source detected by the LMA. When the next LMA point appears, the same charge is placed on it; however the charge placed on the initial point is not removed, but remains. When the third LMA point appears, a new charge is placed on it, while the original two charges are left in place, and so on. In this model, there is no need to distinguish between the beginning of a branch and the end. Every new LMA point gets a δq, and it is left there for the duration of the flash. To conserve charge, an additional positive charge $-\delta q$ is put at the channel origin every time a new δq is added at the new noise point.

[79] The E field for the distributed model is also calculated with equation (15). The results of this model are shown in the dashed plots of Figure 14. For this case, the data were fit with $\delta q = -0.088$ C. There are 261 LMA noise points visible in the figures. Thus the total charge is -23.0 C.

4.2.3. Model and Data Discussion

[80] It is likely that the actual charge distribution falls between the two models. All the charge is not concentrated at the tip of the channel, but neither is it likely spread uniformly along the channel. Note that a considerably smaller charge in the lumped model fits the observed data than the charge required by the distributed model. It is salutary to see that at least the signs, times and approximate magnitudes of the field steps are reproduced by both models. Also, the first rise in modeled E field is larger than the second. Further, the E_x and E_z components are of comparable magnitude in both experiment and model, and the measured component E_y shows much smaller changes than E_x or E_z, in accordance with the model.

[81] One obvious deviation of the models from the data is that the measured E_y component of the electric field rides a negatively sloping background. We attribute this slope to instrument rotation. In the presence of a large constant

transverse field E_T, a rotating Esonde will see the constant field as a slow field change. In fact, electric field meters that rotate to obtain a DC field measurement have a long history, beginning in 1926 [see *Chalmers*, 1967] and references therein) and continuing into the present decade [*Coleman et al.*, 2003]. With additional analysis, it might be possible to calculate the transverse DC component of the electric field from our data. At present, though, we focus on the rapid effects of lightning on the electric field.

[82] The two models above represent extreme charge distributions along a lightning channel. In the lumped model, charges of −4.0 C and −1.0 C propagate at the tips of two channels. In the distributed model, a charge of −0.088 C is placed at each source of radiation detected by the Lightning Mapping Array, for a total of −23.0 C. The modeling attempted to reproduce the electric field components at the location of the balloon-borne instrument in order to learn how charge is distributed along the channels. While the agreement between the field components and the modeled components is fair, the predictions of the two models are strikingly similar: compare the dashed and dotted curves in Figure 14. Thus, even if the modeled electric field components matched the observed components much more closely, we could not distinguish between lumped and distributed charge along the channels.

[83] How could the electric field components at the balloon from a lumped charge of −4 C be so similar to the components from a distributed charge of −23 C? The answer is probably that only the closest charges make a significant contribution to the electric field at the balloon. It appears that the nearest fifty or so charges in the distributed model, amounting to a total of −4 C, are approximately equivalent to the −4 C in the lumped model, and the remaining part of the −23 C is too far away to have much effect. In the case when a lightning flash passes by the balloon-borne instrument, both approaching and receding, then we expect the two models to make substantially different predictions. *Proctor* [1981], with electric field meters on the ground, considered two models similar to ours and concluded that the distributed charge model fit his results better.

5. Conclusion

[84] With a single airborne instrument used in conjunction with the Lightning Mapping Array and the National Lightning Detection Network, it is possible to learn how charge is transported in lightning flashes. In the first example above, a cloud-to-ground flash, the angles of electric vectors at the position of the balloon-borne Esonde show that charge is moved progressively farther from the ground-strike point as each stroke of the flash transfers charge to ground. For the earlier strokes in the flash, while lightning channels are near the ground strike point, simple calculations give the amounts of charge transferred to ground for each stroke.

[85] In the second example, an intracloud flash, two methods of distributing charge along a lightning channel (whose position as a function of time is shown by the LMA) are used in an attempt to reproduce the measured electric vectors at the position of the Esonde. The results do not give a clear indication of how the charge is distributed, but with additional measurements on channels that come closer to the balloon-borne instrument or with more than one Esonde in the air simultaneously, it should be possible to determine the distribution of charge along single channels.

[86] **Acknowledgments.** Everyone at Langmuir Laboratory contributed to this work in some way. Steven Hunyady supported the Langmuir compact LMA. Brian Mong, Mike Stock, Jeff Peischl and Will Walden-Newman integrated, operated and calibrated the instrument. Harald Edens preprocessed the LMA data. Nate Campbell customized the XLMA computer program for this work. Paul Krehbiel, Bill Rison and Ron Thomas provided invaluable aid with LMA data interpretation. Graydon Aulich and Ken Eack provided ballooning assistance and an additional tracking package. Thanks to Candace Lindquist for editorial assistance and many useful discussions, to Sandy Kieft for several types of support, and to Monte Bateman of NASA for sharing his atmospheric electricity reference database. This work was funded primarily by grant ATM-0331164 from the National Science Foundation. Additional funding was provided by the Office of the President of New Mexico Tech, by the Irving and Marion Langmuir bequest to Langmuir Laboratory, and by NASA through the New Mexico Space Grant Consortium. The first author also acknowledges start-up funds from the office of Research and Economic Development at New Mexico Tech. The field operations at Langmuir Laboratory were conducted on the Cibola National Forest under a Special Use Permit from the U.S. Forest Service.

References

Beasley, W. H., K. B. Eack, H. E. Morris, W. D. Rust, and D. R. MacGorman (2000), Electric-field changes of lightning observed in thunderstorms, *Geophys. Res. Lett.*, *27*(2), 189–192.

Chalmers, J. A. (1967), *Atmospheric Electricity*, *Int. Ser. of Monogr. on Nat. Philos.*, vol. 11, 2nd ed., 515 pp., Elsevier, New York.

Coleman, L. M., T. C. Marshall, M. Stolzenburg, T. Hamlin, P. R. Krehbiel, W. Rison, and R. J. Thomas (2003), Effects of charge and electrostatic potential on lightning propagation, *J. Geophys. Res.*, *108*(D9), 4298, doi:10.1029/2002JD002718.

Cramer, J. A., M. J. Murphy, D. Crawford, V. A. Rakov, and K. L. Cummins (2001), An evaluation of the performance characteristics of the NLDN using triggered lightning, *Eos Trans. AGU*, *82*(47), Fall Meet. Suppl., Abstract AE11A–0068.

Few, A. A., and T. L. Teer (1974), The accuracy of acoustic reconstructions of lightning channels, *J. Geophys. Res.*, *79*(33), 5007–5011.

Idone, V. P., D. A. Davis, P. K. Moore, Y. Wang, R. W. Henderson, M. Ries, and P. F. Jamason (1998), Performance evaluation of the U.S. National Lightning Detection Network in eastern New York: 2. Location accuracy, *J. Geophys. Res.*, *103*, 9057–9069.

Krehbiel, P. R., M. Brook, and R. A. McCrory (1979), An analysis of the charge structure of lightning discharges to ground, *J. Geophys. Res.*, *84*(C5), 2432–2456.

Krehbiel, P. R., R. J. Thomas, W. Rison, T. Hamlin, J. Harlin, and M. Davis (2000), GPS-based mapping system reveals lightning inside storms, *Eos Trans. AGU*, *81*(3), 21–25.

MacGorman, D. R., and W. D. Rust (1998), *The Electrical Nature of Storms*, 422 pp., Oxford Univ. Press, New York.

Marshall, T. C., and W. D. Rust (1991), Electric field soundings through thunderstorms, *J. Geophys. Res.*, *96*(D12), 22,297–22,306.

Proctor, D. E. (1981), VHF radio pictures of cloud flashes, *J. Geophys. Res.*, *86*, 4041–4071.

Pugh, E. M., and E. W. Pugh (1970), *Principles of Electricity and Magnetism*, 2nd ed., pp. 102–103, Addison-Wesley, Boston, Mass.

Rison, W., R. J. Thomas, P. R. Krehbiel, T. Hamlin, and J. Harlin (1999), A GPS-based three-dimensional lightning mapping system: Initial observations in central New Mexico, *Geophys. Res. Lett.*, *26*(23), 3573–3576.

Thomas, R. J., P. R. Krehbiel, W. Rison, S. J. Hunyady, W. P. Winn, T. Hamlin, and J. Harlin (2004), Accuracy of the Lightning Mapping Array, *J. Geophys. Res.*, *109*, D14207, doi:10.1029/2004JD004549.

Thomson, E. M., P. J. Medelius, M. Rubenstein, M. A. Uman, J. Johnson, and J. W. Stone (1988a), Horizontal electric fields from lightning return strokes, *J. Geophys. Res.*, *93*(D3), 2429–2441.

Thomson, E. M., P. J. Medelius, and M. A. Uman (1988b), A remote sensor for the three components of transient electric fields, *Proc. IEEE*, *35*, 426–433.

Uman, M. A., et al. (1978), An unusual lightning flash at Kennedy Space Center, *Science*, *201*, 9–16.

J. Battles, Space Instrumentation and Systems Engineering, Los Alamos National Laboratory, Los Alamos, NM 87545, USA.

G. Lu, R. G. Sonnenfeld, and W. P. Winn, Department of Physics and Langmuir Laboratory, New Mexico Tech, 801 Leroy Place, Socorro, NM 87801, USA. (rsonnenf@nmt.edu)